RSC Advances

PAPER

View Article Online
View Journal | View Issue

Cite this: *RSC Adv.*, 2026, **16**, 14054

Unleashing the redox-active mediator effect on the Ni-MOF electrode with a flower-like structure employed for supercapacitor applications

Hanaa A. Mohamedien,[a] Fatma Mohamed, *[b] Soha M. Kamal[a] and Abeer Enaiet Allah [bc]

Improving the energy density and performance of a supercapacitor necessitates the use of novel electrode materials and electrolytes that possess long-term stability. The high energy density, pseudocapacitance, and specific capacitance may be conferred by superior electrodes and redox mediator electrolytes used in the practical application of supercapacitors. In this work, the Ni-BDC MOF was synthesized using a solvothermal method, and its potential for use in supercapacitor applications was examined. Its morphology, microstructure, crystalline phase, and functional groups were determined using SEM coupled with EDX, XRD, and FTIR analyses, respectively. In addition, Brunauer–Emmett–Teller analysis was performed to estimate the catalyst's BET surface area and distribution of pore size. The Ni-BDC MOF electrodes' electrochemical performances were estimated using CV, GCD, and EIS techniques in various aqueous electrolytes (1 M KOH, 1 M H_2SO_4, and 1 M Na_2SO_4) and a redox electrolyte (1 M H_2SO_4 + 0.1 M KI). The Ni-BDC MOF electrode exhibited a high specific capacitance (capacity) of 1569.98 F g^{-1} (852.5 C g^{-1}) at 10 A g^{-1} current density in a 1 M H_2SO_4 + 0.1 M KI electrolyte, with a maximum energy density of 64.29 Wh kg^{-1}, maximum power density of 11 600 W kg^{-1}, and remarkable capacitance retention of 125.49% after 1500 GCD cycles at 80 A g^{-1} current density. Its performance was superior to that in the KI redox electrolyte and conventional KOH, H_2SO_4, and Na_2SO_4 electrolytes. The admirable electrochemical performance of the Ni-BDC MOF in the 1 M H_2SO_4 + 0.1 M KI electrolyte was attributed to the small mass of hydrogen ions (H+).

Received 15th December 2025
Accepted 21st February 2026

DOI: 10.1039/d5ra09485b

rsc.li/rsc-advances

1. Introduction

Increasing pollution levels and the growing demand for energy are the two main issues related to the burning of fossil fuels on a global scale. Therefore, to overcome the challenges that may arise due to the energy crisis and solve the aforementioned concerns, scientists have made many efforts to develop effective technologies and environmentally friendly, renewable, and sustainable energy sources.[1–5] Batteries, fuel cells, and supercapacitors are examples of energy storage devices (ESDs).[5] Supercapacitors (SCs) are a very important example of sustainable and clean energy sources and devices. Supercapacitors are also called electrochemical capacitors and ultracapacitors. They have attracted considerable interest owing to their high cyclic stability, high coulombic efficiency, outstanding power density, and tunable energy density.[1,3,6–10] They can be used in several applications, such as automobiles, braking systems, cellphones, tiny renewable energy devices, solar cells, and wind turbines, because of their aforementioned properties.[11] Depending on the energy storage mechanism, supercapacitors can be categorized into electric double-layer capacitors (EDLC), pseudocapacitors (PCs), and battery-type hybrid capacitors (BTCs).[10,12,13] EDLC storage devices store energy in an electrostatic manner *via* the reversible adsorption of electrolyte ions on the large surface area of electrochemically stable active materials. However, PCs and BTCs store energy through the redox reaction of active surface substances on electrode materials, and Faradaic charge transfer occurs at the electroactive sites on the surface, or a reversible chemical reaction occurs between electrode materials and electrolyte ions; hence, they deliver a higher capacitance, capacity, and energy density than EDLCs.[2,12,13]

Metal–organic frameworks (MOFs) are a novel type of porous inorganic–organic hybrid crystalline material comprising metal ions connected to organic linkers or ligands through coordinate bonds. They have fascinating characteristics and are employed in many different fields, for example, sensors, drug delivery, wastewater treatment, catalysis, gas adsorption, biomedicine, batteries, water splitting, and supercapacitors.[4,9,14–16] MOFs are

[a]*Applied Electrochemistry Laboratory, Chemistry Department, Faculty of Science, Beni-Suef University, Beni-Suef, 62511, Egypt. E-mail: soha.kamel@yahoo.com; hanaaabdelmohsen288@gmail.com*

[b]*Materials Science Lab, Chemistry Department, Faculty of Science, Beni-Suef University, Beni-Suef, 62511, Egypt. E-mail: F_chem2010@yahoo.com*

[c]*Applied Industrial Chemistry Department, Faculty of Science, National Beni Suef University, Egypt. E-mail: abeer.abdelaal@science.bsu.edu.eg*

effective for electrochemical energy storage in supercapacitors owing to their high surface area, controllable micropore structure, structural and functional flexibility, tunable pore size, and possible pseudocapacitive redox centers.[1,4,9,15–17] MOFs can be used as precursors to prepare other materials such as carbon materials, metal oxides, metal phosphides, metal nitrides, and composites.[12]

Ni-MOFs have been employed as supercapacitor electrode materials and have demonstrated effective long-term cycling stability, excellent capacitance, and high rate capability. Wang *et al.* synthesized 3D Ni-MOF microflowers *via* a facile method in a DMF/water/alcohol mixed solvent. The prepared electrode exhibited a maximum capacitance of 1093 F g^{-1} at 1 A g^{-1} using 1 M KOH as an aqueous electrolyte and a nickel foam as a working electrode and maintained 625 F g^{-1} at 5 A g^{-1}, signifying its excellent rate capability owing to its large surface area and hierarchical superstructure.[18] S. Kumar *et al.* fabricated a Ni-MOF on a Cu foam and achieved 534 F g^{-1} in a 3 M KOH electrolyte at 3 A g^{-1}. Moreover, its performance was enhanced through the preparation of a core–shell-structured CuO@Ni-MOF material that exhibited a 1455.74 F g^{-1} specific capacitance.[19] Xiao and his coworkers synthesized a Ni-MOF and achieved a 606.8 F g^{-1} capacitance in a 3 M KOH solution at 1 A g^{-1}. They also constructed GM-LEG@Ni-MOF to improve the obtained capacitance and achieved a 913.9 F g^{-1} capacitance with 85.6% capacity retention after 3000 cycles.[20] Geng Li *et al.* used a carbon cloth substrate to directly prepare Ni-MOF nanosheets and achieved a capacity of 87.6 mA h g^{-1} in a 2 M KOH aqueous electrolyte at 2 mA cm^{-2}. They also loaded Ni-MOF nanosheets onto $NiCo_2O_4$ nanowires to form core–shell hybrid $NiCo_2O_4$@Ni-MOF arrays, which delivered a specific capacity of 208.8 mA h g^{-1} at 2 mA cm^{-2}.[21] Bao and his group synthesized rGO/Ni-MOF. The working electrode was made by coating the prepared slurry on a titanium mesh substrate, and it delivered a capacitance of 160.7 F g^{-1} in 1 M H_2SO_4 at a 0.2 A g^{-1} current density. Moreover, the capacitance was enhanced through the preparation of rGO/Ni-MOF/PANI, which achieved 197.5 F g^{-1}.[22] Raje *et al.* fabricated Ni-MOFs with different molar ratios of Ni and p-benzene dicarboxylic acid (PTA), as a ligand, at different temperatures and times. They achieved a capacitance of 853 F g^{-1} at 10 A g^{-1} in a 1 M KOH electrolyte at a 1 : 1 ratio and a capacitance of 1668.47 F g^{-1} at a 3 : 1 ratio, along with 79% capacitance retention after 10 000 cycles at 100 mV s^{-1}.[23] Edris Jamshidi *et al.* prepared the CoAl-LDH and nickel core–shell-structured nanocomposite (Ni@CoAl-LDH). They achieved capacitances of 341.75 F g^{-1} for CoAl-LDH and 792.5 F g^{-1} for the Ni@CoAl-LDH nanocomposite at 1 A g^{-1} in a 1 M KOH electrolyte using a nickel foam substrate.[24]

The employment of a redox-additive substance in a standard electrolyte, for example, H_2SO_4, KOH, and Na_2SO_4, at the ideal concentration is one of the key strategies to enhance the supercapacitor performance through quick reversible redox reaction which leads to increasing capacitance and energy density. Redox additive electrolytes can be organic, such as hydroquinone,[25,26] or inorganic, such as potassium iodide (KI),[26,27] potassium bromide (KBr),[28] potassium ferricyanide ($K_3[Fe(CN)_6]$),[29,30] potassium ferrocyanide ($K_4[Fe(CN)_6]$),[31] sodium sulphides (Na_2S),[32] thiourea,[33] sodium molybdate (Na_2MoO_4),[34] vanadyl sulfate ($VOSO_4$),[35] and ammonium metavanadate (NH_4VO_3),[36] and they have already been tested by many researchers to enhance the capacitance and energy density of electrodes. Jiang *et al.* enhanced the CuZnNi–MOF electrode's capacitance using a 3 M KOH + 0.05 M $K_4Fe(CN)_6$ mixed electrolyte and achieved a 112.5 mA h g^{-1} specific capacity (837 F g^{-1}).[31] Sandhiya *et al.* enhanced the capacitance of SSG carbon-based supercapacitors from 375 F g^{-1} to 658 F g^{-1} at 3 A g^{-1} through the addition of NH_4VO_3 to the H_2SO_4 electrolyte.[36] Abbasi and coworkers prepared nitrogen-doped porous carbon spheres (N-PCS) and achieved a capacitance of 775.5 F g^{-1} at 1 A g^{-1} in 1 M H_2SO_4 + 50 mM KI.[37] Senthilkumar *et al.* prepared biomass-derived activated carbon using complex steps such as cutting of *Eichhornia crassipes* into small pieces, drying in sunlight, grinding, preheating to remove moisture, activation using $ZnCl_2$ for 24 h, carbonization at different temperatures in an Ar atmosphere, washing with distilled water, and finally overnight drying. They used it as a supercapacitor electrode in a 1 M H_2SO_4 solution, which delivered a 472 F g^{-1} specific capacitance at 2 mA cm^{-2}, and an enhanced capacitance of 912 F g^{-1} was achieved by adding 0.08 M KI to the 1 M H_2SO_4 aqueous electrolyte, but the obtained energy density was 19.04 Wh kg^{-1}, which was not desirable.[38]

Previous research works have achieved fairly good results, but some of them use complicated methods for the preparation of the electrode active material, which consume a lot of time and energy; hence, they are not desirable. Moreover, MOFs synthesized without any additional annealing process are still not widely employed as electrode materials in supercapacitors (SCs).[7] Thus, in this study, we provide a simple solvothermal technique for the effective preparation of the Ni-BDC MOF by utilizing the organic ligand 1,4-benzenedicarboxylic acid (BDC) at a low reaction temperature without any subsequent complicated processes and with a low energy-consuming annealing process. The as-prepared Ni-BDC MOF is characterized by SEM, EDX, XRD, BET, and FTIR analyses. The pseudo and battery-like materials are electrolyte-dependent as they are only electrochemically active in specific electrolytes; hence, the electrochemical properties of the Ni-BDC MOF electrode are studied using the cyclic voltammetry (CV) technique, galvanostatic charge/discharge (GCD) method, and electrochemical impedance spectroscopy (EIS) method in various conventional electrolytes (1 M KOH, 1 M H_2SO_4, and 1 M Na_2SO_4 electrolytes). Furthermore, iodide ions are very promising redox mediators because they have several redox states (for example, I^-, I_3^- and IO_3^-), which are formed during the charge/discharge process and readily enter the micropores and/or tiny mesopores on the electrode's surface because of their small ionic size, leading to the appearance of redox peaks in CV, a large faradaic plateau in charge–discharge profiles, and hence an enhancement in the ionic conductivity of the electrolyte. Moreover, this is the first report on using the Ni-BDC MOF as a supercapacitor electrode in a H_2SO_4 conventional electrolyte with a KI redox additive electrolyte. The Ni-BDC MOF electrode delivers a maximum specific capacitance of 1569.98 F g^{-1} at a current density of 10 A g^{-1} in the 1 M H_2SO_4 + 0.1 M KI electrolyte, an excellent

cycling stability of 125.49% at 80 A g^{-1} after 1500 GCD cycles, a maximum power density of 11 600 W kg^{-1}, and a maximum energy density of 64.29 Wh kg^{-1}.

This work is inspired by the urgent need to develop high-performance, low-cost, and facilely synthesized electrode materials for next-generation supercapacitors. Although Ni-based metal–organic frameworks (Ni-MOFs) have shown promising electrochemical properties, many reported approaches rely on complicated synthesis routes, post-treatments, or composite formation, which increase the cost, time, and energy consumption while limiting practical scalability. In addition, the electrochemical performance of MOF electrodes is strongly dependent on the electrolyte system, and the role of redox-mediator electrolytes in enhancing charge storage mechanisms remains insufficiently explored, particularly in acidic media.

Therefore, this study aims to (i) synthesize a flower-like Ni-BDC MOF using a simple solvothermal method without any postannealing or complex processing, (ii) systematically investigate its electrochemical behavior in different conventional aqueous electrolytes, and (iii) explore the redox-mediator effect of KI in the H_2SO_4 electrolyte to significantly enhance the capacitance, energy density, and cycling stability. This work seeks to provide a practical strategy for improving MOF-based supercapacitor electrodes through simultaneous material design and electrolyte engineering.

2. Experimental section

2.1. Materials and chemicals

Nickel chloride hexahydrate ($NiCl_2 \cdot 6H_2O$) was bought from LOBA Chemie. Benzene dicarboxylic acid (BDC) was obtained from Central Drug House (P) Ltd. *N*,*N*-Dimethyl formamide (DMF) was purchased from CARLO ERBA. Ethanol (C_2H_5OH) and potassium hydroxide pellets (KOH) were purchased from ISOLAB Chemicals. Sodium sulphate (Na_2SO_4) was purchased from POWER CHEMICAL. Sulphuric acid (H_2SO_4) was purchased from Pio Chem. Potassium iodide (KI) was obtained from TECHNO PHARMCHEM (TPC), and a Nafion 117 solution was purchased from Sigma-Aldrich.

2.2. Synthesis of the Ni-BDC MOF

The Ni-BDC MOF was made through a simple solvothermal process. First, 0.7131 g of $NiCl_2 \cdot 6H_2O$ and 0.498 g of benzene dicarboxylic acid (BDC) were separately dissolved in 20 mL of *N*,*N*-dimethyl formamide (DMF) and then stirred. Second, the BDC solution was added to the nickel chloride solution dropwise, stirred for 10 min, and ultrasonicated for 1 h at ambient temperature. Finally, the mixture was poured into a 60 mL Teflon-lined stainless-steel autoclave kettle for 22 h at 150 °C. The obtained sample was collected on a filter paper and washed three times with DMF and methanol under stirring for 60 minutes. Finally, the precipitate was dried at 80 °C overnight.

2.3. Characterization

The Ni-BDC MOF material's morphology was characterized using scanning electron microscopy analysis (SEM, JEOL Ltd, JSM-IT200, Tokyo, Japan). Moreover, the Ni-BDC MOF material's elemental composition was investigated *via* EDX coupled with SEM. Powder X-ray diffraction (PXRD) was performed using an X-ray diffractometer (JSX-60 PA, Japan) with a wavelength of 1.5418 Å and Cu Ka radiation to explore the crystalline structure of the prepared material. Using a Tri-Star II 3020 (Micromeritics, USA) analyzer, the Ni-BDC MOF material's surface area and pore size distribution were investigated through N_2 adsorption–desorption isotherms using the Brunauer–Emmett–Teller (BET) method. The Fourier transform infrared (FTIR) spectrum of the Ni-BDC MOF material was recorded using a Vertex 70 (Bruker, Germany) spectrometer in the wavenumber range of 4000–400 cm^{-1} to verify the synthesis of the Ni-BDC MOF and determine the present functional groups.

2.4. Electrochemical measurements

The Ni-BDC MOF electrodes' electrochemical properties were investigated using a three-electrode setup, in which the counter electrode was a platinum wire, the reference electrode was Ag/AgCl, and a graphite sheet current collector was the working electrode (WE). They were tested using various electrolytes, such as 1 M KOH (basic), 1 M H_2SO_4 (acidic), and 1 M Na_2SO_4 (neutral), and a redox additive 1 M H_2SO_4 + 0.1 M KI electrolyte. The graphite sheet working electrodes (WEs) with a 1 cm^2 active surface area were prepared by diffusing 1 mg of the prepared material in 200 μL of a mixed solvent of isopropanol/water (1 : 2 v/v) (containing 10 μL of the Nafion 117 solution), followed by sonication at an ambient temperature to create a homogenous ink, which was dropped onto the graphite WE and dried at a temperature of 60 °C. A potentiostat/galvanostat (AUTOLAB PGSTAT 302N, Metrohm, Switzerland) with NOVA 1.11 software was used to perform the Ni-BDC MOF electrodes' electrochemical measurements, such as cyclic voltammetry (CV) and galvanostatic charge/discharge (GCD), within a potential window suitable for each electrolyte. Electrochemical impedance spectroscopy (EIS) was performed in the frequency range of 0.01 Hz to 100 kHz with an amplitude of 10 mV AC.

The Ni-BDC MOF electrodes' specific gravimetric capacitances were calculated from the CV curves by applying eqn (1),[39–41] and its specific capacities (Q_s) were calculated using eqn (2):[42]

$$C_s = (\int i\mathrm{d}V)/(2mv\Delta V) \quad (1)$$

$$Q_s = (\int i\mathrm{d}V)/(2mv) \quad (2)$$

where C_s represents the specific capacitance (F g^{-1}), Q_s represents the specific capacity (C g^{-1}), $\int i\mathrm{d}V$ is the CV curve integration area (AV), m represents the active material's mass (g), v represents the scan rate (V s^{-1}), and ΔV denotes the potential window (V).

The Ni-BDC MOF electrodes' gravimetric specific capacitances (C_s) and specific capacities (Q_s) were computed from

GCD curves using eqn (3) and (4), respectively.[39,43–45] The energy and power densities of the Ni-BDC MOF electrode were calculated according to eqn (5) and (6), respectively.[43,45,46]

$$C_s = (It)/(m\Delta V) \quad (3)$$

$$Q_s = It/m \quad (4)$$

$$E = (C_s \Delta V^2)/(2 \times 3.6) \quad (5)$$

$$P = 3600E/\Delta t \quad (6)$$

here, C_s denotes the specific capacitance (F g^{-1}), Q_s represents the specific capacity (C g^{-1}), I represents the current (A), t represents the discharge time (s), m is the active material's mass (g), with excluding the IR drop, ΔV is the potential change during the discharge process (V) with excluding the IR drop, E is the energy density (Wh kg^{-1}) and P is the power density (W kg^{-1}).

3. Results and discussions

3.1. Structural characterization

3.1.1. Scanning electron microscopy (SEM). The morphology of the Ni-BDC MOF was characterized by SEM at different magnifications and is displayed in Fig. 1a and b. The Ni-BDC MOF material has a flower-like morphology with a hydrangea-like microspherical structure. Fig. 1b presents the high-magnification SEM image and shows that the flowers are composed of nanosheets that are vertically aligned and cross each other, leading to the presence of gaps between them. These gaps can hold a significant volume of electrolyte, allowing it to sufficiently permeate the interior of the nanospheres, facilitating the transport of electrolyte ions and electrons, which enhances the Ni-BDC MOF material's electrochemical performance for application in various energy storage devices. Moreover, the EDX spectrum was measured to determine the Ni-BDC MOF material's elemental composition. The analysis results

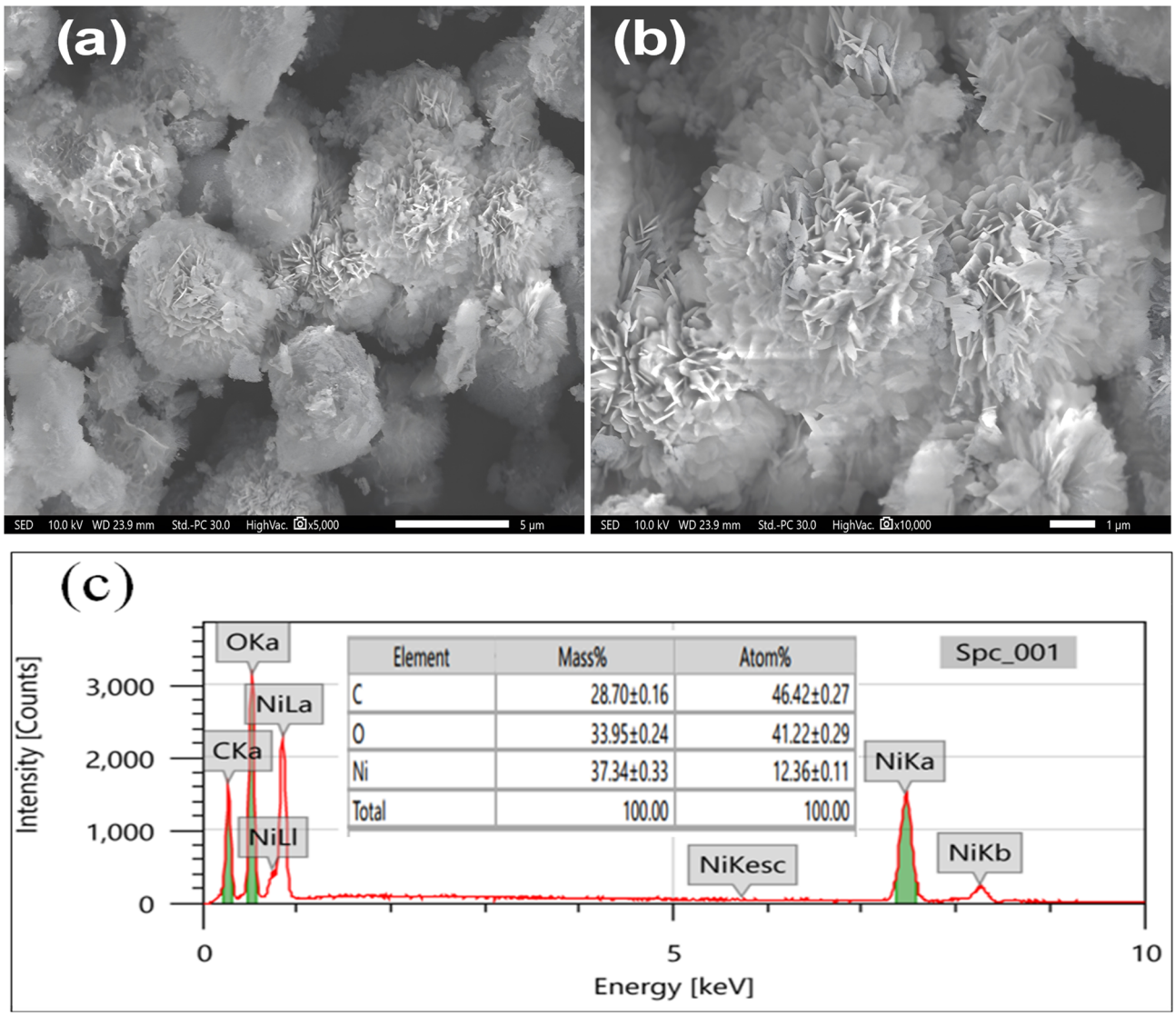

Fig. 1 SEM images (a and b) of the Ni-BDC MOF material at different magnifications and (c) EDX analysis of the Ni-BDC MOF material and its elemental composition.

suggest that C, O, and Ni elements are present in the sample, as displayed in Fig. 1c.

3.1.2. Powder X-ray diffraction (PXRD). The crystalline structure of the Ni-BDC MOF catalyst and its composition were examined through powder X-ray diffraction and are shown in Fig. 2a. The material shows a peak at $2\theta = 8.6°$, which is characteristic of MOFs with BDC ligands (CCDC no. 690314).[47,48] Furthermore, the PXRD pattern of the Ni-BDC MOF is similar to the simulated pattern of the Ni-MOF reported in the literature[49–58] and also to those of Ni-MOFs prepared in previous studies.[48,49,57] The peaks at $2\theta = 8.6°$, 16° and 17.2° are correlated to the (100), (010), and (101) planes, respectively, and match completely with the $[Ni_3(OH)_2(C_8H_4O_4)_2(H_2O)_4]\cdot 2H_2O$ (CCDC no. 638866) single-crystal data. Moreover, the (100) plane of the studied sample is detected as the largest exposed plane.[48,59] The peaks at $2\theta = 44.44°$, 51.9°, and 76.5° are correlated to the (111), (200), and (220) Ni planes (JCPDS no. 89-7128), respectively.[60,61]

3.1.3. Brunauer–Emmet–Teller (BET). The Ni-BDC MOF material's surface area and porosity were determined through the BET technique, in addition to performing nitrogen adsorption–desorption isotherm analysis, as demonstrated in Fig. 2b (the inset is the graph of the pore size distribution). The N_2 adsorption–desorption isotherm of the Ni-BDC MOF exhibited a type-IV adsorption isotherm and a H3 hysteresis loop, verifying that the Ni-BDC MOF catalyst had a mesoporous structure (mesopore diameter = 2–50 nm).[62–67] The Ni-BDC MOF material had an average pore size of 13.25404 nm and a pore volume of 0.397440 $cm^3\ g^{-1}$. The Ni-BDC MOF material's calculated BET surface area was found to be 119.9454 $m^2\ g^{-1}$, which is higher than that of the majority of previously documented porous Ni-MOFs.[15,23,65,66] This large surface area offers a large contact area and highly reactive sites at the electrolyte–electrode interface, which facilitate quick ion transport, provide space for electrons, and afford the electrode material high electrochemical performance.[64,66] The pore size distribution of the Ni-BDC MOF material, determined *via* the BJH method, is presented in the inset of Fig. 2b. The presence of pores with diameters 3.43, 6.34, and 8.63 nm, which signify a mesoporous-type structure, was evident. The mesopores offer pathways and channels for the diffusion and movement of ions and electrons, which enhances the electrochemical performance.[66]

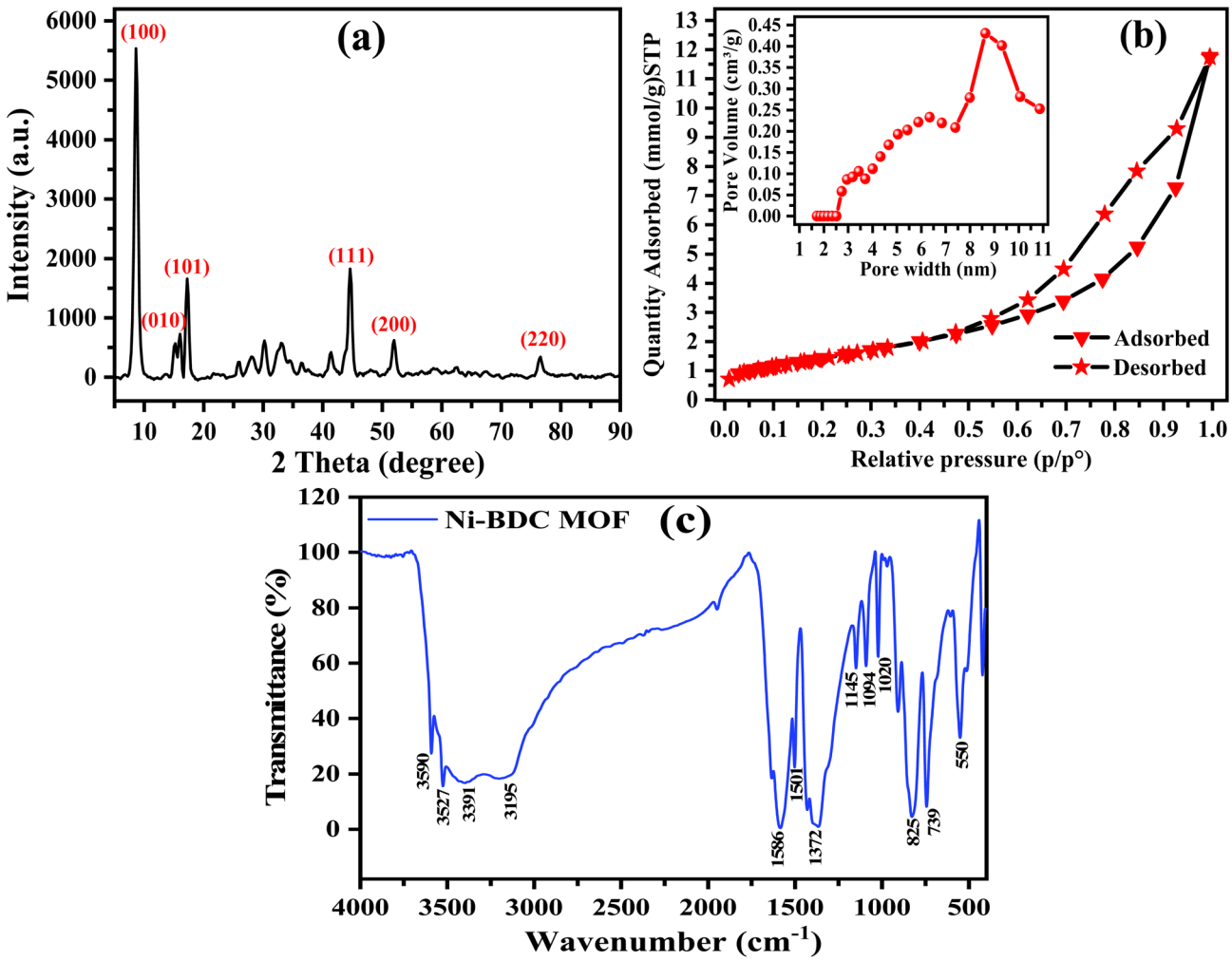

Fig. 2 (a) XRD pattern, (b) nitrogen adsorption–desorption isotherms (inset: pore size distribution graph), and (c) FTIR spectrum of the Ni-BDC MOF material.

3.1.4. Fourier transform infrared (FTIR) spectroscopy. The Fourier transform infrared (FTIR) spectrum of the Ni-BDC MOF material is displayed in Fig. 2c. The peaks at 1586 and 1372 cm^{-1} were ascribed to the asymmetric and symmetric stretching vibrations of the $-COO^-$ group, respectively, which implied the coordination of this group of the H_2BDC bidentate ligand with the Ni^{2+} ion.[20,66,68] The peaks at 1094 and 1145 cm^{-1} were related to C–C stretching vibrations.[22] The presence of coordinated water molecules in the Ni-BDC MOF material was proven by the presence of stretching vibration bands at 3195, 3391, 3527, and 3590 cm^{-1} (a broad band at 3600–3000 cm^{-1}),[20,66,68–70] which were also related to the overlapped

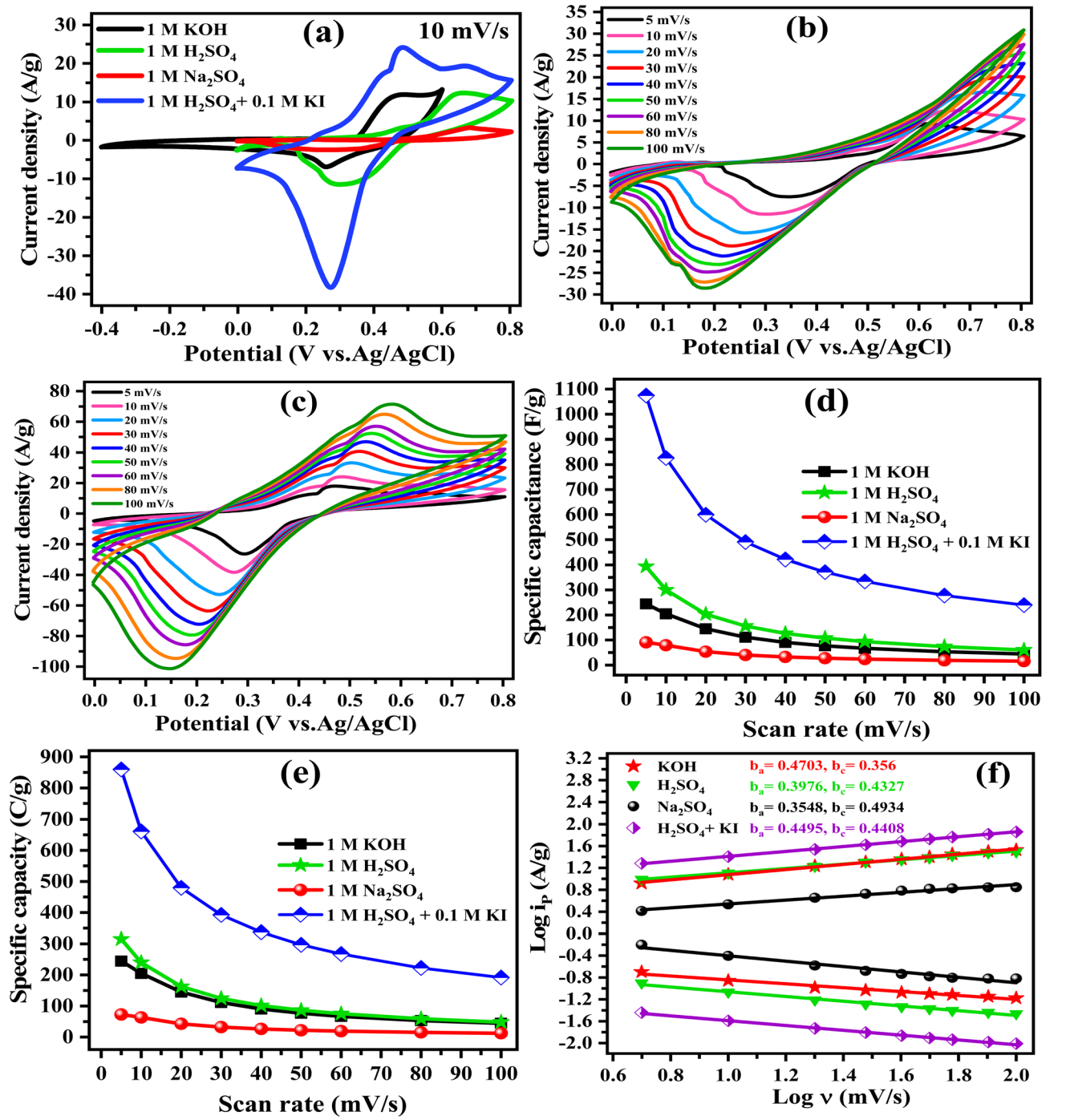

Fig. 3 (a) Cyclic voltammetry (CV) curves of the Ni-BDC MOF electrodes at a 10 mV s^{-1} scan rate in different electrolytes (1 M KOH, 1 M H_2SO_4, 1 M Na_2SO_4, and 1 M H_2SO_4 + 0.1 M KI), (b) CV curves at different scan rates in a 1 M H_2SO_4 electrolyte, (c) CV curves at different scan rates in a 1 M H_2SO_4 + 0.1 M KI electrolyte, (d) specific capacitance (F g^{-1}) in different electrolytes as a function of the scan rate, (e) specific capacity (C g^{-1}) in different electrolytes as a function of the scan rate, and (f) logarithmic plot of anodic and cathodic peak current densities (log i_p) *versus* scan rate (log υ) in different electrolytes.

stretching vibrations of various oxygen functional groups such as –H_2O, –OH, or –COOH and their molecular hydrogen bonding.[71] The peaks at 1020 and 739 cm^{-1} were attributed to C–O and C–H stretching vibrations, respectively, while the peak at 550 cm^{-1} was attributed to the stretching vibration of the Ni–O bond, which confirmed the existence of Ni ions in the material.[19] The peak at 1501 cm^{-1} represented the vibrational stretching of the *para*-aromatic C–H group,[68] and that at 825 cm^{-1} was assigned to the out-of-plane C–H bending of the para-substituted benzene ring, which confirmed the structure of the H_2BDC ligand, which was used in the preparation of MOFs. Furthermore, the absence of a peak at 1670 cm^{-1} confirmed the absence of the free H_2BDC ligand in the analyzed MOF material.[72]

3.2. Electrochemical performance study

The Ni-BDC MOF electrodes' electrochemical performances were analyzed in a three-electrode system using the cyclic voltammetry (CV) technique, galvanostatic charge/discharge (GCD) method, and electrochemical impedance spectroscopy (EIS), which were performed in various electrolytes such as 1 M KOH, 1 M H_2SO_4, 1 M Na_2SO_4 and 1 M H_2SO_4 + 0.1 M KI electrolytes. Fig. 3a displays the Ni-BDC MOF electrodes' CV curves at a 10 mV s^{-1} scan rate in various electrolytes and different potential windows suitable for each electrolyte. The potential was increased until a sharp rise in the current was seen in the CV curve, which clearly indicated that the electrolyte was breaking down. The potential window for the Ni-BDC MOF electrode was obtained in the 1 M KOH electrolyte (−0.4 V to 0.6 V) and compared to that in 1 M H_2SO_4 (0 V to 0.8 V), 1 M Na_2SO_4 (0 V to 0.8 V), and 1 M H_2SO_4 + 0.1 M KI (0 V to 0.8 V) electrolytes. Clearly, all CV curves revealed a redox peak pair originating from the faradaic redox reactions between Ni^{2+} and Ni^{3+}, demonstrating the redox behavior and faradaic battery-type features of the studied material. Furthermore, the integrated CV curve area and maximum current in the H_2SO_4 electrolyte were larger than those in KOH and Na_2SO_4 electrolytes, suggesting the highest electrochemical performance and hence expected capacitance, which is also supported by the longer discharge times in the GCD curves. The Ni-BDC MOF electrode exhibited the best performance and the highest capacitance in the H_2SO_4 electrolyte owing to the lower mass of hydrogen ions (H^+) compared to the higher mass of potassium and sodium ions (K^+ and Na^+), which lowered diffusion kinetics and resistance in the H_2SO_4 electrolyte compared to KOH and Na_2SO_4 electrolytes. We added the KI redox additive electrolyte to the main electrolyte, H_2SO_4, owing to its good performance compared with that of KOH and Na_2SO_4 electrolytes. The addition of KI redox additive electrolyte results in very obvious redox peaks compared to the conventional H_2SO_4 electrolyte, and also the highest integrated area due to the additional multiple redox reactions of $3I^-/I_3^-$, $2I^-/I_2$, $2I_3^-/I_2$, I_2/IO_3^- redox pairs leading to the highest electrochemical performance compared to other electrolytes. The Ni-BDC MOF electrodes' CV curves in H_2SO_4 and 1 M H_2SO_4 + 0.1 M KI electrolytes at different scan rates are shown in Fig. 3b and c, while those in KOH and Na_2SO_4 electrolytes are displayed in Fig. S1, respectively. As the sweep rate increased from 5 to 100 mV s^{-1}, the peak current and integrated area increased, demonstrating the fast transfer rates of electrons and ions as a result of the reversible redox reactions occurring between the Ni-BDC MOF electrode and electrolyte. Furthermore, anodic peaks moved to higher positive voltages, while the cathodic peaks moved to negative potentials, indicating the electrode's polarization effect and the quick charge/discharge rate of the reversible redox reactions of Ni-BDC MOF electrode material. The diffusion-controlled battery-type behavior of any material can be verified through the disappearance of the oxidation peak at high scan rates in various electrolytes,[73] while the maintenance of the CV curve's shape in the case of the redox additive at high scan rates signified the great capacity, small resistance, and high stability of the electrode.[74] The Ni-BDC MOF electrodes' specific capacitances and capacities were calculated at different scan rates in all studied electrolytes using eqn (1) and (2), respectively, as presented in Fig. 3d and e. It is clearly observed that the H_2SO_4 electrolyte afforded a higher specific capacitance and capacity than KOH, which was higher than those in the Na_2SO_4 electrolyte thanks to the lower mass of hydrogen ions (H^+) than that of potassium and sodium ions (K^+ and Na^+), which resulted in lower diffusion kinetics and resistance in the H_2SO_4 electrolyte. Moreover, the addition of the redox electrolyte increased the capacitance and capacity compared to other electrolytes. At a 5 mV s^{-1} scan rate, the Ni-BDC MOF electrode delivered specific capacitances (capacities) of 244.32 F g^{-1} (244.32 C g^{-1}), 393.86 F g^{-1} (315.1 C g^{-1}), 90.94 F g^{-1} (72.75 C g^{-1}), and 1074.61 F g^{-1} (859.69 C g^{-1}) in KOH, H_2SO_4, Na_2SO_4, and H_2SO_4 + KI electrolytes, respectively. Furthermore, the capacitance decreased with increasing sweep rate due to the insufficiency of time for the deep penetration of electrolyte ions into the inner layers of the electrode at high scan rates. As a result, redox reactions only happened on the electrode's active outer surface. The possible electrochemical redox reactions that occurred in the case of the KI redox additive electrolyte are as follows:[26,37,75]

$$3I^- \leftrightarrow I_3^- + 2e^- \quad (7)$$

$$2I^- \leftrightarrow I_2 + 2e^- \quad (8)$$

$$2I_3^- \leftrightarrow 3I_2 + 2e^- \quad (9)$$

$$I_2 + 6H_2O \leftrightarrow 2IO_3^- + 12H^+ + 10e^- \quad (10)$$

To evaluate the charge storage mechanism of the Ni-BDC MOF electrode in different studied electrolytes, the relationship between the current density (i, A g^{-1}) and scan rate (υ, mV s^{-1}) was studied according to the following equations:

$$i = a\upsilon^b \quad (11)$$

$$\log i = \log a + b \log \upsilon \quad (12)$$

where a and b represent constants. Specifically, when the b value is 0.5, the diffusion process is predominantly responsible for controlling charge storage. Conversely, surface capacitance generally regulates charge storage when $b = 1$. Moreover, when b is between 0.5 and 1, both surface capacitance and diffusion processes control charge storage. Logarithmic calculations established from the cathodic and anodic currents of the studied electrode in different electrolytes are shown in Fig. 3f. The b values were obtained from the slope of the log i_p linear fit curves against log v. From the figure, it is evident that b values calculated from both anodic (b_a) and cathodic (b_c) peak currents in the various studied electrolytes were lower than 0.5

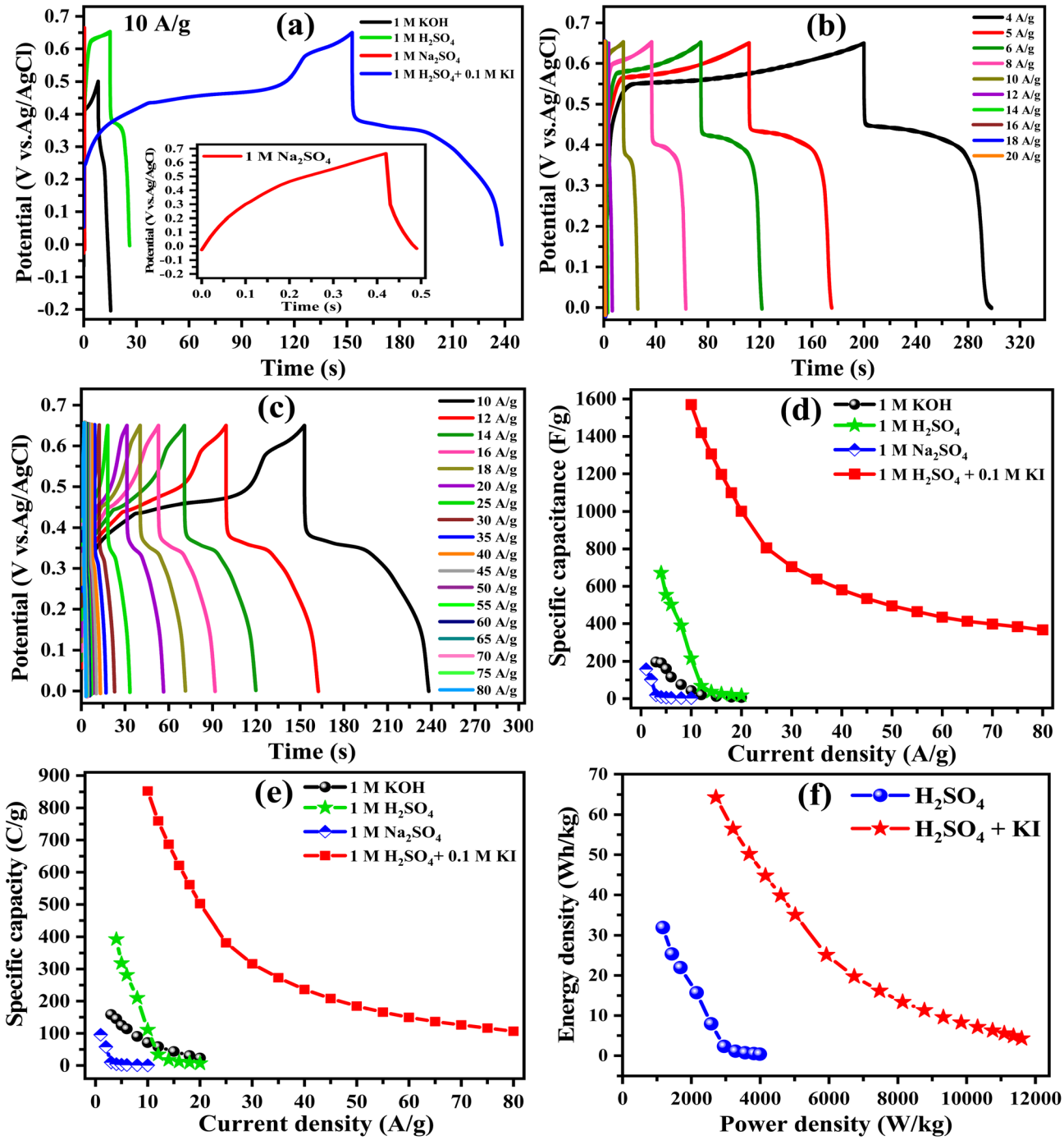

Fig. 4 (a) Galvanostatic charge–discharge (GCD) curves of the Ni-BDC MOF electrodes in different electrolytes (1 M KOH, 1 M H_2SO_4, 1 M Na_2SO_4, and 1 M H_2SO_4 + 0.1 M KI) at a current density of 10 A g^{-1} (inset is the GCD curve in a 1 M Na_2SO_4 electrolyte), (b) GCD curves at different current densities in 1 M H_2SO_4, (c) GCD curves at different current densities in a 1 M H_2SO_4 + 0.1 M KI electrolyte, (d) specific capacitance (F g^{-1}) *versus* current densities, (e) specific capacity (C g^{-1}) *versus* current densities, and (f) Ragone plots of the Ni-BDC MOF electrode in H_2SO_4 and H_2SO_4 + KI electrolytes.

Table 1 Comparison of the specific capacitance or capacity, cyclic stability, energy density, power density, electrolyte, used ligand, and morphology of the Ni-BDC MOF electrode and other reported electrodes in various aqueous electrolytes and redox electrolytes using a three-electrode system

Materials	Ligand	Substrate	Electrolyte	Specific capacitance (F g^{-1}) or capacity (C g^{-1}), current density	Stability (%), *n* cycles	Energy density (Wh kg^{-1})	Power density (W kg^{-1})	Ref.
Ni-MOF nanoflower-like structure	Benzene-1,4-dicarboxylic acid and hexamethylenetetramine	Carbon felt (CF)	1 M NaOH	623.7 F g^{-1}, 6 mA cm^{-2}	73%, 3000 (50 mA cm^{-2})	88.4	4300	83
Ni-MOF nanorod-like morphology	Trimesic acid (BTC)	Stainless-steel mesh	2 M KOH	1956.3 F g^{-1}, 5 mA cm^{-2}	81.13%, 3000 (35 mA cm^{-2})	—	—	69
Binder-free Ni-MOF nanosheets	1,4-Benzenedicarboxylic acid (1,4-BDC)	Stainless steel	1 M KOH	850.42 F g^{-1}, 1 mA cm^{-2}	70.2%, 1500 (1 mA cm^{-2})	18.66	1671	81
Ni-MOF layered cuboid	1,4-Benzenedicarboxylic acid (H_2BDC)	Ni foam	2 M KOH	432 F g^{-1}, 1 A g^{-1}	60.48%, 5000 (10 A g^{-1})	—	—	80
Ni-MOF nanosheets	Trimesic acid	Carbon	3 M KOH	1057.2 F g^{-1}, 1 A g^{-1}	70%, 2500 (10 A g^{-1})	—	—	15
Ni-MOF nanospheres	Trimesic acid	FTO glass	1 M LiOH	230 F g^{-1}, 0.42 A g^{-1}	53%, 1000	32	311	66
Ni-MOF nanospheres	Trimesic acid	FTO glass	1 M NaOH	212 F g^{-1}, 0.42 A g^{-1}	85%, 1000	31	245	66
Ni-MOF nanospheres	Trimesic acid	FTO glass	1 M KOH	283 F g^{-1}, 0.42 A g^{-1}	154%, 1000	48	467	66
Ni-MOF nanosheets	Terephthalic acid (PTA)	Ni foam	6 M KOH	721 F g^{-1}, 1 A g^{-1}	61%, 3000 (5 A g^{-1})	—	—	82
Ni-MOF albizia flower-like spheres	Trimesic acid (BTC) and terephthalic acid (PTA)	Ni foam	6 M KOH	920 F g^{-1}, 1 A g^{-1}	80%, 3000 (5 A g^{-1})	—	—	82
Ni-MOF nanoflower	2-Methylimidazole	Ni foam	6 M KOH	467 C g^{-1}, 1 A g^{-1}	83%, 5000 (5 A g^{-1})	—	—	65
RGO/Ni-MOF sphere-flake-sphere structure	Trimesic acid (TMA)	Ni-coated polyester fabric	6 M KOH	64.3 F g^{-1}, 4 mA cm^{-2}	80%, 2000 (8 mA cm^{-2})	—	—	79
Ni-MOF-derived nickel phosphide/carbon composite nanosphere of (Ni_xP_y) with a carbon framework	Terephthalic acid (TPA)	Graphite foil	1 M Na_2SO_4 + 0.2 M $K_3[Fe(CN)_6]$	2136.3 F g^{-1}, 3 A g^{-1}	90.6, 5000 (10 A g^{-1})	52.5	758	78
CuZnNi-MOF	Benzene dicarboxylic acid (H_2BDC) and 1,4-diazabicyclo-[2.2.2]-octane (dabco)	Ni foam	3 M KOH + 0.05 M $K_4Fe(CN)_6$	837 F g^{-1} (112.5 mAh g^{-1}), 1 A g^{-1}	47.9%, 5000 (8 A g^{-1})	—	—	31
ZIF-67/GNPs	2-Methylimidazole (MIM)	Glassy carbon (GC)	1 M Na_2SO_4 + 0.2 M $[K_3(Fe(CN)_6)]$	1573 F g^{-1}, 8 A g^{-1}	97.7%, 10 000 (1 A g^{-1})	85.8	7500	29
Ni-MOF microflowers	1,4-Benzene dicarboxylic acid (BDC)	Graphite sheet	1 M KOH	196.24 F g^{-1}, 3 A g^{-1}	—	14.87	1014	This work
Ni-MOF microflowers	1,4-Benzene dicarboxylic acid (BDC)	Graphite sheet	1 M H_2SO_4	671.25 F g^{-1}, 4 A g^{-1}	—	31.91	1170	This work
Ni-MOF microflowers	1,4-Benzene dicarboxylic acid (BDC)	Graphite sheet	1 M Na_2SO_4	158.11 F g^{-1}, 1 A g^{-1}	—	8.01	302	This work
Ni-MOF microflowers	1,4-Benzene dicarboxylic acid (BDC)	Graphite sheet	1 M H_2SO_4 + 0.1 M KI	1569.98 F g^{-1}, 10 A g^{-1}	125.49%, 1500 (80 A g^{-1})	64.29	2715	This work

(b < 0.5), signifying that the diffusion-controlled process dominated charge storage, which was suggested by the linearity of the graphs.[76]

The galvanostatic charge–discharge (GCD) technique was used to estimate the Ni-BDC MOF electrodes' specific capacitances and capacities in various electrolytes at different current densities. Fig. 4a displays a comparison of the Ni-BDC electrodes' GCD curves at 10 A g^{-1} in different electrolytes. The electrode exhibited a longer discharge time in the H_2SO_4 electrolyte than in KOH and Na_2SO_4 electrolytes, signifying the highest specific capacitance in the H_2SO_4 solution. Moreover, after the addition of the KI redox additive to the H_2SO_4 solution, the discharge time increased due to additional redox reactions, signifying the highest capacitance among them. The charge/discharge (GCD) curves displayed a nonlinear behavior, which established the presence of redox peaks in CV curves. The GCD curves of the Ni-BDC MOF electrode in H_2SO_4 and H_2SO_4 + KI electrolytes at different current densities are presented in Fig. 4b and c, respectively, and those in the presence of KOH and Na_2SO_4 electrolytes are presented in Fig. S2. As exhibited by Fig. 4b and c, the GCD graphs displayed a nonlinear behavior. The time consumed (*e.g.*, at 10 A g^{-1}) in the case of the H_2SO_4 + KI electrolyte was higher than that in the H_2SO_4 electrolyte, indicating the better performance and hence the better capacitance in the presence of the redox additive. In addition, the discharge time decreased with increasing current density owing to the inadequate faradaic reaction of active materials within a limited time (insufficient time for the redox reactions), the increased resistance, and the involvement of only the electrode's active outer surface in the redox reaction at high current densities.[77] Fig. 4d and e exhibit the Ni-BDC MOF electrodes' specific capacitances and capacities in different electrolytes, which were estimated from GCD curves at different current densities according to eqn (3) and (4), respectively. Ni-BDC MOF electrodes exhibited capacitances (capacities) of 114.49 F g^{-1} (71.1 C g^{-1}), 215.34 F g^{-1} (110.9 C g^{-1}), 3.03 F g^{-1} (0.9 C g^{-1}), and 1569.98 F g^{-1} (852.5 C g^{-1}) at 10 A g^{-1} in the presence of KOH, H_2SO_4, Na_2SO_4, and H_2SO_4 + KI electrolytes, respectively. Moreover, the maximum calculated specific capacitance (capacity) values of Ni-BDC MOF electrode materials in the presence of H_2SO_4 + KI electrolyte are 1569.98 F g^{-1} (852.5 C g^{-1}) at 10 A g^{-1}, 671.25 F g^{-1} (392.68 C g^{-1}) at 4 A g^{-1} for H_2SO_4 electrolyte, 234.28 F g^{-1} (158.37 C g^{-1}) at 3 A g^{-1} in KOH electrolyte, and 158.11 F g^{-1} (95.5 C g^{-1}) at 1 A g^{-1} for Na_2SO_4 electrolyte. Both capacitances and capacities were high at low current densities owing to the existence of micropores and/or mesopores for ion transport and charge storage.[3] Furthermore, the values of capacitances and capacities decreased with increasing current density because only the electrode's active outer surface participated in the redox reaction at high current densities. In addition, the different studied electrolytes had different capacitance retentions owing to the different ionic masses for each electrolyte, and the electrolyte ions did not have sufficient time to fully enter the active electrode material's internal pores at higher current densities. Additionally, the Ni-BDC MOF electrodes' energy densities (EDs) and power densities (PDs) in the H_2SO_4 solution and H_2SO_4 + KI redox electrolyte were calculated using eqn (5) and (6), respectively. As displayed in Fig. 4f, the Ni-BDC MOF electrode exhibited a maximum ED of 64.29 Wh kg^{-1} at 2715 W kg^{-1} PD while demonstrating a maximum PD of 11 600 W kg^{-1} at an ED of 4.29 Wh kg^{-1} in the H_2SO_4 + KI redox electrolyte, compared to 31.91 Wh kg^{-1} at 1170 W kg^{-1} and 0.39 Wh kg^{-1} at 3990 W kg^{-1} in the H_2SO_4 electrolyte. The specific capacitance or capacity, cyclic stability, energy density, power density, electrolyte, used ligand, and morphology of the as-prepared Ni-BDC MOF electrode were compared to those of some previously reported electrode

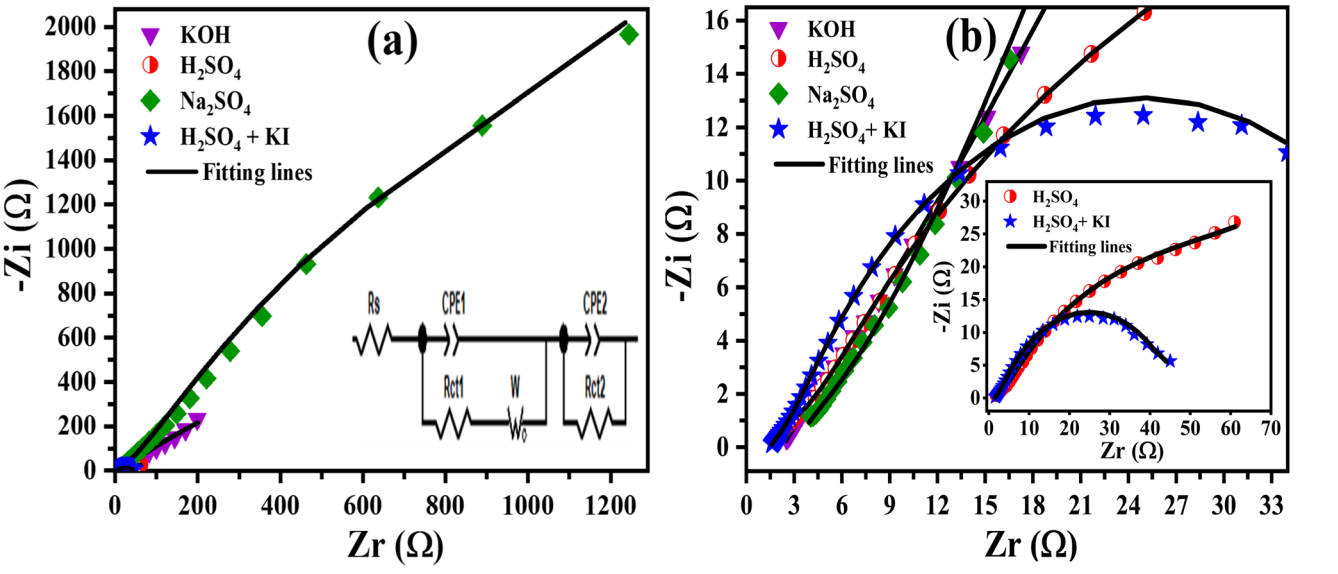

Fig. 5 (a) Nyquist plots of the Ni-BDC MOF electrodes in different electrolytes (the inset is the equivalent circuit diagram fitted for data obtained from all electrolytes except the redox electrolyte) and (b) magnified view of the Nyquist plots (inset shows the Nyquist plots of the Ni-BDC MOF electrodes in H_2SO_4 and H_2SO_4 + KI electrolytes).

materials using a threeelectrode system, as exhibited in Table 1.[15,29,31,65,66,69,78–83]

Electrochemical impedance spectroscopy (EIS) is an effective method for determining the electrochemical behavior and resistance of the studied electrode in different electrolytes. Fig. 5a demonstrates the corresponding Nyquist plots of the Ni-BDC MOF electrode in various electrolytes, and the inset shows the equivalent circuit (EC) applied to fit the EIS spectra in all electrolytes, except the H_2SO_4 + KI redox electrolyte. We used the EC to determine electrochemical parameters such as internal resistance (R_s), charge transfer resistance (R_{ct}), constant phase element (CPE) and Warburg impedance (W), respectively, as presented in Table S1. Fig. 5b presents a magnified view of Nyquist plots in the high-frequency region, and the inset shows the Nyquist plots obtained in H_2SO_4 and H_2SO_4 + KI electrolytes. Generally, in the high-frequency region, the Nyquist plots showed similar shapes without a noticeable semicircle, indicating quick electron transport kinetics and very small charge transfer resistance of the electrode/electrolyte interface.[3,84] Nyquist plots also showed a spike in the lower-frequency region, which denotes the electrolyte ions' diffusion to the surface of the electrode (Warburg resistance, W). Additionally, R_s, comprising the electrolyte resistance, the contact resistance of the electrode/electrolyte interface, and the intrinsic resistance of the electroactive substance, was determined by crossing with the real axis in the high-frequency region. The R_s and R_{ct} values vary with the used electrolyte. The R_s was determined to be 2.247 Ω, 1.399 Ω, and 2.975 Ω and the R_T ($R_T = R_{ct1} + R_{ct2}$) was computed to be 917.73 Ω, 79.28 Ω, and 4740.157 Ω in KOH, H_2SO_4, and Na_2SO_4 electrolytes, respectively. The lowest R_s and R_T values of the Ni-BDC MOF material in the H_2SO_4 electrolyte indicated low resistance, high electrical conductivity, quicker electron transfer and a high ion diffusion rate at the electrode/electrolyte interface thanks to the smallest size of the H^+ ion, which contributes to the supercapacitor's improved electrochemical performance. Furthermore, the equivalent circuit (EC) used to fit the EIS spectrum in the presence of the redox additive electrolyte is displayed in the inset of Fig. 6c. The shape of the Nyquist plot for the Ni-BDC MOF electrode in the H_2SO_4 + KI redox electrolyte was different from that in other studied electrolytes, and consequently, the electrochemical equivalent circuit also changed. The values of R_s and R_T were 1.486 Ω and 45.696 Ω, respectively. The total charge transfer resistance (R_T) was less than that obtained in the conventional H_2SO_4 electrolyte due to the increase in the electrolyte's ionic conductivity and the consequent decrease in the resistivity when the redox additive (KI) was added to the conventional H_2SO_4 electrolyte.[26]

The Ni-BDC MOF electrode's cycling stability was analyzed in a three-electrode configuration in the 1 M H_2SO_4 + 0.1 M KI electrolyte at 80 A g^{-1} for 1500 galvanostatic charge–discharge (GCD) cycles, as displayed in Fig. 6a. The capacitance progressively increased, achieving a retention of 125.49% of its initial capacitance value after 1500 GCD cycles, possibly because of the exposure of active sites to electrolyte ions and additional redox reactions from the redox additive electrolyte, and leading to electrode activation through the gradual penetration of the

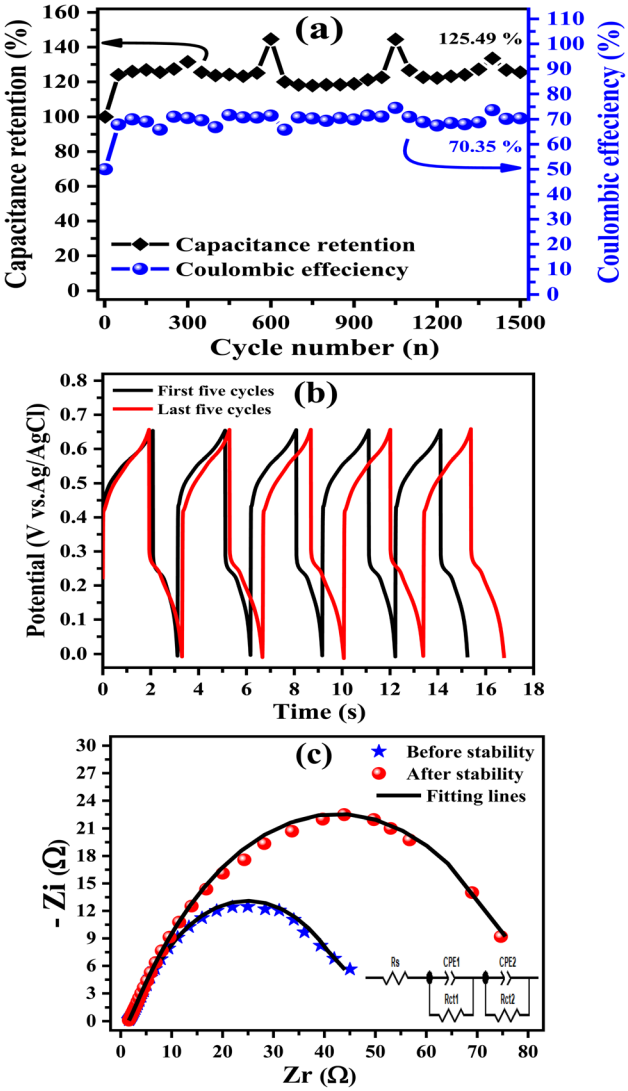

Fig. 6 (a) Cycling stability and coulombic efficiency of the Ni-BDC MOF electrode in a H_2SO_4 + KI redox electrolyte at 80 A g^{-1} for 1500 GCD cycles, (b) first and last five GCD cycles of the Ni-BDC MOF electrode at 80 A g^{-1}, and (c) Nyquist plots of the Ni-BDC MOF electrode in a H_2SO_4 + KI redox electrolyte before and after stability tests (inset is the equivalent circuit diagram).

electrolyte ions into the material's pores. This demonstrates the good stability and excellent long-term durability of the electrode even at high current density.[85–87] The capacitance retention of our material exceeded that of other previously documented materials, as displayed in Table 1. Moreover, the coulombic efficiency remained 70.35% after 1500 GCD cycles. Furthermore, a comparison of the first and last five cycles of the entire cycling test is shown in Fig. 6b. The shape of the last 5 cycles remained almost the same as that of the first five cycles, verifying the exceptional electrochemical performance and stability of the electrode. Additionally, the last five cycles consumed more time than the first five cycles, confirming the improvement in performance and capacitance retention and good stability.

To learn more about the electrochemical properties, EIS measurements of the Ni-BDC MOF electrode were carried out before and after 1500 GCD cycles in the 1 M H_2SO_4 + 0.1 M KI electrolyte, as shown in Fig. 6c, and the inset shows the electrochemical equivalent circuit (EC) fitted to the data. The Nyquist plots before and after the cycling stability test had the same shapes with a slight variation in the parameter values obtained from EC, implying the good cycling stability of the electrode. The R_s value increased slightly from 1.486 Ω to 1.516 Ω. Moreover, the R_T ($R_T = R_{ct1} + R_{ct2}$) value increased from 45.696 Ω to 80.96 Ω, implying the accumulation of electrolyte ions during the stability test.

4. Conclusion

In brief, a facile solvothermal method for the preparation of the Ni-BDC MOF as a supercapacitor electrode material in different electrolytes was presented. The synthesis of the Ni-BDC MOF flower-like material was successfully verified using the XRD and FTIR data. The Ni-BDC MOF material's BET surface area, average pore size and pore volume were 119.9454 $m^2\ g^{-1}$, 13.25404 nm, and 0.397440 $cm^3\ g^{-1}$, respectively. The electrochemical characteristics of the Ni-BDC MOF material were evaluated through CV, GCD, and EIS techniques. Compared to the other electrolyte solutions (1 M KOH and 1 M Na_2SO_4), the 1 M H_2SO_4 electrolyte delivered a superior capacitance of 671.25 F g^{-1} at 4 A g^{-1}. The highest specific capacitance of 1569.98 F g^{-1} was achieved for the studied redox additive electrolyte (1 M H_2SO_4 + 0.1 M KI) at 10 A g^{-1}, along with a 125.49% capacitance retention at 80 A g^{-1} after 1500 GCD cycles. Additionally, a maximum energy density of 64.29 Wh kg^{-1} was achieved at a power density of 2715 W kg^{-1}. The findings indicate that the Ni-BDC MOF is a suitable electrode material for high-performance supercapacitors. It is expected that the simple synthesis method presented here would open an avenue for creating various MOF-based materials with superior electrochemical properties for energy conversion and storage applications.

Conflicts of interest

There are no conflicts of interset to declare.

Data availability

The data supporting this article have been included as part of the supplementary information (SI). Supplementary information is available. See DOI: https://doi.org/10.1039/d5ra09485b.

References

1 M. Saleem, F. Ahmad, M. Fatima, A. Shahzad, M. S. Javed, S. Atiq, M. A. Khan, M. Danish, O. Munir, S. M. Bin Arif, U. Faryad, M. J. Shabbir and D. Khan, Exploring new frontiers in supercapacitor electrodes through MOF advancements, *J. Energy Storage*, 2024, **76**, 109822, DOI: 10.1016/j.est.2023.109822.

2 C. K. Roy, S. S. Shah, A. H. Reaz, S. Sultana, A. N. Chowdhury, S. H. Firoz, M. H. Zahir, M. A. Ahmed Qasem and M. A. Aziz, Preparation of Hierarchical Porous Activated Carbon from Banana Leaves for High-performance Supercapacitor: Effect of Type of Electrolytes on Performance, *Chem.–Asian J.*, 2021, **16**, 296–308, DOI: 10.1002/asia.202001342.

3 S. Sundriyal, V. Shrivastav, A. Kaur, Mansi, A. Deep and S. R. Dhakate, Surface and diffusion charge contribution study of neem leaves derived porous carbon electrode for supercapacitor applications using acidic, basic, and neutral electrolytes, *J. Energy Storage*, 2021, **41**, 103000, DOI: 10.1016/j.est.2021.103000.

4 I. Rabani, J. W. Lee, T. Lim, H. B. Truong, S. Nisar, S. Afzal and Y. S. Seo, Construction of a uniform zeolitic imidazole framework (ZIF-8) nanocrystal through a wet chemical route towards supercapacitor application, *RSC Adv.*, 2024, **14**, 118–130, DOI: 10.1039/d3ra06941a.

5 A. Shahmohammadi, S. Dalvand, A. Molaei, S. M. Mousavi-Khoshdel, N. Yazdanfar and M. Hasanzadeh, Transition metal phosphide/molybdenum disulfide heterostructures towards advanced electrochemical energy storage: recent progress and challenges, *RSC Adv.*, 2025, **15**, 13397–13430, DOI: 10.1039/d5ra01184a.

6 Y. Liu, S. Li, C. Wang, L. Guo and Y. Wang, Accordion-like bimetal-organic framework anchoring on the partially-exfoliated graphite paper for high-performance supercapacitors, *Appl. Surf. Sci.*, 2020, **528**, 146954, DOI: 10.1016/j.apsusc.2020.146954.

7 S. Weng, Q. An, Y. Xu, Y. Jiao and J. Chen, In-Situ Formation of NiFe-MOF on Nickel Foam as a Self-Supporting Electrode for Flexible Electrochemical Sensing and Energy Conversion, *Chemosensors*, 2023, **11**(4), 242, DOI: 10.3390/chemosensors11040242.

8 P. Lamba, P. Singh, P. Singh, P. Singh, Bharti, A. Kumar, M. Gupta and Y. Kumar, Recent advancements in supercapacitors based on different electrode materials: Classifications, synthesis methods and comparative performance, *J. Energy Storage*, 2022, **48**, 103871, DOI: 10.1016/j.est.2021.103871.

9 R. Naz, M. Arslan Raza, K. Tul Kubra, S. Mehboob, M. Farooq Khan and G. Ali, ZIF-67 and titania derived quaternary composites as electrode materials for high-performance supercapacitor, *J. Ind. Eng. Chem.*, 2024, **136**, 188–200, DOI: 10.1016/j.jiec.2024.02.006.

10 R. Velayutham, R. Manikandan, C. Justin Raj, A. Dennyson Savariraj, W. J. Cho, H. M. Jang and B. Chul Kim, Rationally designed metal–organic framework templated iron-molybdenum sulfide for high energy density hybrid supercapacitors, *Appl. Surf. Sci.*, 2021, **570**, 151051, DOI: 10.1016/j.apsusc.2021.151051.

11 E. E. Sauerbrei, R. Faggiani and C. Calvo, Effects of Co-doping on the microstructure and electrochemical performance of nickel vanadate (Ni3V2O8) electrode material for aqueous symmetric supercapacitor, *Inorg. Chem. Commun.*, 2024, **170**, 113209, DOI: 10.1107/s0567740873006552.

12 J. Zhao, L. Yang, R. Li and Y. Zhou, One−Step Synthesis of Fe−Based Metal–Organic Framework (MOF) Nanosheet Array as Efficient Cathode for Hybrid Supercapacitors, *Inorganics*, 2023, **11**(4), 169, DOI: 10.3390/inorganics11040169.

13 B. A. Ali, A. H. Biby and N. K. Allam, Toward the Proper Selection of Carbon Electrode Materials for Energy Storage Applications: Experimental and Theoretical Insights, *Energy Fuels*, 2021, **35**, 13426–13437, DOI: 10.1021/acs.energyfuels.1c01528.

14 D. Yu, Q. Shao, Q. Song, J. Cui, Y. Zhang, B. Wu, L. Ge, Y. Wang, Y. Zhang, Y. Qin, R. Vajtai, P. M. Ajayan, H. Wang, T. Xu and Y. Wu, A solvent-assisted ligand exchange approach enables metal-organic frameworks with diverse and complex architectures, *Nat. Commun.*, 2020, **11**, 927, DOI: 10.1038/s41467-020-14671-9.

15 P. Du, Y. Dong, C. Liu, W. Wei, D. Liu and P. Liu, Fabrication of hierarchical porous nickel based metal-organic framework (Ni-MOF) constructed with nanosheets as novel pseudo-capacitive material for asymmetric supercapacitor, *J. Colloid Interface Sci.*, 2018, **518**, 57–68, DOI: 10.1016/j.jcis.2018.02.010.

16 Q. Yin, T. Xu, F. Cao, Y. Wang, C. Yang, N. Liu, J. Liu and R. Liu, Heterostructures of NiFe-MOF/PBAs with high-performance supercapacitors obtained by compounding Prussian blue analogues on bimetallic organic frames, *Electrochim. Acta*, 2024, **476**, 143749, DOI: 10.1016/j.electacta.2023.143749.

17 T. A. Hamdalla, S. Alfadhli, S. Khasim, A. A. A. Darwish, E. F. M. ElZaidia, S. A. Al-Ghamdi, M. M. Aljohani, M. E. Mahmoud and S. M. Seleim, Synthesis of novel Cu/Fe based benzene Dicarboxylate (BDC) metal organic frameworks and investigations into their optical and electrochemical properties, *Heliyon*, 2024, **10**, e25065, DOI: 10.1016/j.heliyon.2024.e25065.

18 C. H. Wang, D. W. Zhang, S. Liu, Y. Yamauchi, F. B. Zhang and Y. V. Kaneti, Ultrathin nanosheet-assembled nickel-based metal–organic framework microflowers for supercapacitor applications, *Chem. Commun.*, 2022, **58**, 1009–1012, DOI: 10.1039/d1cc04880e.

19 S. Kumar, P. H. Weng and Y. P. Fu, Core-shell-structured CuO@Ni-MOF: bifunctional electrode toward battery-type supercapacitors and oxygen evolution reaction, *Mater. Today Chem.*, 2022, **26**, 101159, DOI: 10.1016/j.mtchem.2022.101159.

20 Y. Xiao, W. Wei, M. Zhang, S. Jiao, Y. Shi and S. Ding, Facile Surface Properties Engineering of High-Quality Graphene: Toward Advanced Ni-MOF Heterostructures for High-Performance Supercapacitor Electrode, *ACS Appl. Energy Mater.*, 2019, **2**, 2169–2177, DOI: 10.1021/acsaem.8b02201.

21 G. Li, H. Cai, X. Li, J. Zhang, D. Zhang, Y. Yang and J. Xiong, Construction of Hierarchical NiCo2O4@Ni-MOF Hybrid Arrays on Carbon Cloth as Superior Battery-Type Electrodes for Flexible Solid-State Hybrid Supercapacitors, *ACS Appl. Mater. Interfaces*, 2019, **11**, 37675–37684, DOI: 10.1021/acsami.9b11994.

22 Q. B. Le, H. Fei, C. Bubulinca, F. A. Ngwabebhoh, N. E. Kazantseva and P. Saha, Reduced Graphene Oxide Composited with Ni-MOF and PANI Applied as Electrodes for Supercapacitor, *ECS Trans.*, 2020, **99**, 93–101, DOI: 10.1149/09901.0093ecst.

23 P. G. Raje, S. R. Gurav, M. R. Waikar, G. R. Chodankar, U. V. Shembade, A. V. Moholkar, T. D. Dongale and R. G. Sonkawade, Exploring the role of metal concentrations on the chemically synthesized Ni-MOFs nanostructures for asymmetric supercapacitor, *J. Energy Storage*, 2024, **95**, 112617, DOI: 10.1016/j.est.2024.112617.

24 E. Jamshidi, S. Dalvand, F. Manteghi and S. M. Mousavi-Khoshdel, A cobalt-aluminium layered double hydroxide with a nickel core-shell structure nanocomposite for supercapacitor applications, *IScience*, 2025, **28**, 111672, DOI: 10.1016/j.isci.2024.111672.

25 D. D. Zhai, H. Liu, M. Wang, D. Wu, X. Y. Chen and Z. J. Zhang, Integrating surface functionalization and redox additives to improve surface reactivity for high performance supercapacitors, *Electrochim. Acta*, 2019, **323**, 134810, DOI: 10.1016/j.electacta.2019.134810.

26 M. L. Aparna, G. R. Rao and T. Thomas, Momordica Charantia pericarp derived activated carbon with dual redox additive electrolyte for high energy density supercapacitor devices, *J. Energy Storage*, 2022, **48**, 104048, DOI: 10.1016/j.est.2022.104048.

27 Z. Gao, L. Zhang, J. Chang, Z. Wang, D. Wu, F. Xu, Y. Guo and K. Jiang, Catalytic electrode-redox electrolyte supercapacitor system with enhanced capacitive performance, *Chem. Eng. J.*, 2018, **335**, 590–599, DOI: 10.1016/j.cej.2017.11.037.

28 M. Maher, S. Hassan, K. Shoueir, B. Yousif and M. E. A. Abo-Elsoud, Activated carbon electrode with promising specific capacitance based on potassium bromide redox additive electrolyte for supercapacitor application, *J. Mater. Res. Technol.*, 2021, **11**, 1232–1244, DOI: 10.1016/j.jmrt.2021.01.080.

29 A. Akram, M. A. Liaqat, S. Javed, M. Hamid, U. Ali, F. Javed, M. Wei and M. A. Akram, Ultrahigh performance asymmetric supercapacitor devices with synergetic interaction between metal organic frameworks/graphene nano platelets and redox additive electrolyte, *J. Alloys Compd.*, 2022, **891**, 161961, DOI: 10.1016/j.jallcom.2021.161961.

30 H. B. Krishnan, H. N. Lim, I. Ibrahim, M. H. Wahid and C. Y. Foo, Enhancement of energy density for iron MOF-derived composite for aqueous supercapacitor by K3 [Fe(CN)6] redox additive electrolyte, *J. Alloys Compd.*, 2024, **1002**, 175403, DOI: 10.1016/j.jallcom.2024.175403.

31 X. Jiang, S. Deng, J. Liu, N. Qi and Z. Chen, Enhanced Electrochemical Performance of Bimetallic Doped Ni-Based Metal-Organic Frameworks by Redox Additives in an Alkaline Electrolyte, *ACS Appl. Energy Mater.*, 2021, **4**, 4610–4619, DOI: 10.1021/acsaem.1c00230.

32 Z. Q. He, D. D. Chen, M. Wang, C. X. Li, X. Y. Chen and Z. J. Zhang, Sulfur modification of carbon materials as well as the redox additive of Na2S for largely improving capacitive performance of supercapacitors, *J. Electroanal.*

Chem., 2020, **856**, 113678, DOI: 10.1016/j.jelechem.2019.113678.

33 X. Zhang, L. Gao, R. Guo, T. Hu and M. Ma, Using thiourea as a catalytic redox-active additive to enhance the performance of pseudocapacitive supercapacitors, *Sustainable Energy Fuels*, 2021, **5**, 5733–5740, DOI: 10.1039/d1se01129d.

34 B. J. Choudhury, H. H. Muigai, P. Kalita and V. S. Moholkar, Biomass blend derived porous carbon for aqueous supercapacitors with commercial-level mass loadings and enhanced energy density in redox-active electrolyte, *Appl. Surf. Sci.*, 2022, **601**, 154202, DOI: 10.1016/j.apsusc.2022.154202.

35 P. R. Kasturi, R. Harivignesh, Y. S. Lee and R. K. Selvan, Hydrothermally derived porous carbon and its improved electrochemical performance for supercapacitors using redox additive electrolytes, *J. Phys. Chem. Solids*, 2020, **143**, 109447, DOI: 10.1016/j.jpcs.2020.109447.

36 M. Sandhiya, Vivekanand, S. Suresh Balaji and M. Sathish, Unrevealed Performance of NH4VO3 as a Redox-Additive for Augmenting the Energy Density of a Supercapacitor, *J. Phys. Chem. C*, 2021, **125**, 8068–8079, DOI: 10.1021/acs.jpcc.0c11581.

37 S. Abbasi, F. Hekmat and S. Shahrokhian, Dual redox electrolytes for improving the performance of asymmetric supercapacitors constructed from heteroatom-doped green carbon spheres, *J. Alloys Compd.*, 2023, **957**, 170452, DOI: 10.1016/j.jallcom.2023.170452.

38 S. T. Senthilkumar, R. K. Selvan, Y. S. Lee and J. S. Melo, Electric double layer capacitor and its improved specific capacitance using redox additive electrolyte, *J. Mater. Chem. A*, 2013, **1**, 1086–1095, DOI: 10.1039/c2ta00210h.

39 R. Xin, M. Kim, P. Cheng, A. Ashok, S. Chowdhury, T. Park, A. Alowasheeir, M. S. Hossain, J. Tang, J. W. Yi, Y. Yamauchi, Y. V. Kaneti and J. Na, Enlarging the porosity of metal-organic framework-derived carbons for supercapacitor applications by a template-free ethylene glycol etching method, *J. Mater. Chem. A*, 2022, **11**, 12759–12769, DOI: 10.1039/d2ta06307g.

40 M. Anwar, E. W. Cochran, S. Zulfiqar, M. F. Warsi, I. Shakir and K. Chaudhary, In-situ fabricated copper-holmium co-doped cobalt ferrite nanocomposite with cross-linked graphene as novel electrode material for supercapacitor application, *J. Energy Storage*, 2023, **72**, 108438, DOI: 10.1016/j.est.2023.108438.

41 M. R. Biradar, A. V. Salkar, P. P. Morajkar, S. V. Bhosale and S. V. Bhosale, Designing neurotransmitter dopamine-functionalized naphthalene diimide molecular architectures for high-performance organic supercapacitor electrode materials, *New J. Chem.*, 2021, **45**, 9346–9357, DOI: 10.1039/d1nj00269d.

42 S. Sharma and P. Chand, Fabrication of ultrahigh-performance asymmetrical supercapacitor with pristine Zeolitic Imidazolate Framework-8 and a redox additive electrolyte, *Mater. Sci. Semicond. Process.*, 2023, **158**, 107383, DOI: 10.1016/j.mssp.2023.107383.

43 J. Xing, J. Du, X. Zhang, Y. Shao, T. Zhang and C. Xu, Ni-P@NiCo LDH core-shell nanorod-decorated nickel foam with enhanced areal specific capacitance for high-performance supercapacitors, *Dalton Trans.*, 2017, **46**, 10064–10072, DOI: 10.1039/c7dt01910f.

44 X. Han, H. Xuan, J. Gao, T. Liang, J. Yang, Y. Xu, P. Han and Y. Du, Construction of manganese-cobalt-sulfide anchored onto rGO/Ni foam with a high capacity for hybrid supercapacitors, *Electrochim. Acta*, 2018, **288**, 31–41, DOI: 10.1016/j.electacta.2018.08.063.

45 M. R. Pallavolu, S. A. Thomas, J. Cherusseri, B. A. Al-Asbahi, H. T. Das, S. Adem and S. W. Joo, Scalable synthesis of binder-free hierarchical MnCo2O4 nanospikes/Ni(OH)2 nanosheets composite electrodes for high-capacity supercapatteries, *J. Energy Storage*, 2023, **73**, 108999, DOI: 10.1016/j.est.2023.108999.

46 G. Surender, F. S. Omar, S. Bashir, M. Pershaanaa, S. Ramesh and K. Ramesh, Growth of nanostructured cobalt sulfide-based nanocomposite as faradaic binder-free electrode for supercapattery, *J. Energy Storage*, 2021, **39**, 102599, DOI: 10.1016/j.est.2021.102599.

47 K. Yue, J. Liu, C. Xia, K. Zhan, P. Wang, X. Wang, Y. Yan and B. Y. Xia, Controllable synthesis of multidimensional carboxylic acid-based NiFe MOFs as efficient electrocatalysts for oxygen evolution, *Mater. Chem. Front.*, 2021, **5**, 7191–7198, DOI: 10.1039/d1qm00960e.

48 J. Yang, P. Xiong, C. Zheng, H. Qiu and M. Wei, Metal-organic frameworks: A new promising class of materials for a high performance supercapacitor electrode, *J. Mater. Chem. A*, 2014, **2**, 16640–16644, DOI: 10.1039/c4ta04140b.

49 Q. Liu, L. Xie, X. Shi, G. Du, A. M. Asiri, Y. Luo and X. Sun, High-performance water oxidation electrocatalysis enabled by a Ni-MOF nanosheet array, *Inorg. Chem. Front.*, 2018, **5**, 1570–1574, DOI: 10.1039/c7qi00808b.

50 J. Tan, X. He, F. Yin, B. Chen, X. Liang, G. Li and H. Yin, Fe doped metal organic framework (Ni)/carbon black nanosheet as highly active electrocatalyst for oxygen evolution reaction, *Int. J. Hydrogen Energy*, 2020, **45**, 21431–21441, DOI: 10.1016/j.ijhydene.2020.05.230.

51 Y. Han, J. Zhou, L. Wang, L. Xing, Z. Xue, Y. Jiao and Y. Pang, Redox-active nanostructure electrode of Mn/Ni bimetal organic frameworks anchoring on multi-walled carbon nanotubes for advanced supercapacitor, *J. Electroanal. Chem.*, 2021, **882**, 114993, DOI: 10.1016/j.jelechem.2021.114993.

52 J. Lv, P. Liu, F. Yang, L. Xing, D. Wang, X. Chen, H. Gao, X. Huang, Y. Lu and G. Wang, 3D Hydrangea Macrophylla-like Nickel−Vanadium Metal−Organic Frameworks Formed by Self-Assembly of Ultrathin 2D Nanosheets for Overall Water Splitting, *ACS Appl. Mater. Interfaces*, 2020, **12**, 48495–48510, DOI: 10.1021/acsami.0c11722.

53 M. Kashif, S. Thangarasu, N. Murugan, S. S. Magdum, Y. A. Kim, M. Kurkuri and T. H. Oh, Interatomic interaction of 2D crumpled V2O5 nanosheets layered with Ni-MOF as a bifunctional electrocatalyst for overall water splitting and supercapacitor applications, *J. Energy Storage*, 2024, **81**, 110348, DOI: 10.1016/j.est.2023.110348.

54 H. W. Lin, D. Senthil Raja, X. F. Chuah, C. T. Hsieh, Y. A. Chen and S. Y. Lu, Bi-metallic MOFs possessing

hierarchical synergistic effects as high performance electrocatalysts for overall water splitting at high current densities, *Appl. Catal., B*, 2019, **258**, 118023, DOI: 10.1016/j.apcatb.2019.118023.

55 Y. Liu, X. Li, Q. Sun, Z. Wang, W. H. Huang, X. Guo, Z. Fan, R. Ye, Y. Zhu, C. C. Chueh, C. L. Chen and Z. Zhu, Freestanding 2D NiFe Metal–Organic Framework Nanosheets: Facilitating Proton Transfer via Organic Ligands for Efficient Oxygen Evolution Reaction, *Small*, 2022, **18**, 1–10, DOI: 10.1002/smll.202201076.

56 W. Dong, Z. Liu, H. Sun, Z. Shi and J. Xu, Ultrathin defect-rich nanosheets of NiFe-MOF with high specific capacitance and stability for supercapacitor, *Mater. Today Chem.*, 2024, **36**, 101938, DOI: 10.1016/j.mtchem.2024.101938.

57 S. Salehi, M. H. Ehsani and M. Aghazadeh, Direct electrosynthesis of Ni-, Co-, and Ni,Co-MOF onto porous support for high-performance supercapacitors, *J. Alloys Compd.*, 2023, **940**, 168885, DOI: 10.1016/j.jallcom.2023.168885.

58 H. Zhao, L. Zhang, L. Dai, F. Yao, Y. Huang, J. Deng, Y. Fu, J. Zhu and J. Sun, Regulating the transformation behavior of nickel iron metal–organic frameworks through a dual-ligand strategy for enhanced oxygen evolution reaction performance, *Appl. Surf. Sci.*, 2022, **592**, 153252, DOI: 10.1016/j.apsusc.2022.153252.

59 E. Sadeghi, N. S. Peighambardoust, S. Chamani and U. Aydemir, Designing In Situ Grown Ternary Oxide/2D Ni-BDC MOF Nanocomposites on Nickel Foam as Efficient Electrocatalysts for Electrochemical Water Splitting, *ACS Mater. Au*, 2023, **3**, 143–163, DOI: 10.1021/acsmaterialsau.2c00073.

60 J. Li, S. Ma, Z. Qi, J. Ding, M. Yin, B. Zhao, Z. Zhang, Y. Wang, H. Zhang, L. Wang and D. D. Dionysiou, Insights into the removal of chloramphenicol by electrochemical reduction on Pd/NiFe-MOF/foam-Ni electrode: Performance and mechanism, *Appl. Catal., B*, 2023, **322**, 122076, DOI: 10.1016/j.apcatb.2022.122076.

61 J. Yang, J. Guo, X. Guo and L. Chen, In-situ growth carbon nanotubes deriving from a new metal-organic framework for high-performance all-solid-state supercapacitors, *Mater. Lett.*, 2019, **236**, 739–742, DOI: 10.1016/j.matlet.2018.11.062.

62 Z. Yan, H. Qi, X. Bai, K. Huang, Y. R. Chen and Q. Wang, Mn doping of cobalt oxynitride coupled with N-rGO nanosheets hybrid as a highly efficient electrocatalyst for oxygen reduction and oxygen evolution reaction, *Electrochim. Acta*, 2018, **283**, 548–559, DOI: 10.1016/j.electacta.2018.06.185.

63 J. W. Wang, Y. X. Ma, X. Y. Kang, H. J. Yang, B. L. Liu, S. S. Li, X. D. Zhang and F. Ran, A novel moss-like 3D Ni-MOF for high performance supercapacitor electrode material, *J. Solid State Chem.*, 2022, **309**, 122994, DOI: 10.1016/j.jssc.2022.122994.

64 A. M. Kale, M. R. Biradar, W. J. Cho, C. Kaya, S. V. Bhosale, S. V. Bhosale and B. C. Kim, Unveiling a cutting-edge bi-ligand nickel metal-organic framework as an electrode material for symmetric supercapacitors, *J. Energy Storage*, 2023, **73**, 109123, DOI: 10.1016/j.est.2023.109123.

65 A. M. Kale, R. Manikandan, C. Justin Raj, A. Dennyson Savariraj, C. Voz and B. C. Kim, Protonated nickel 2-methylimidazole framework as an advanced electrode material for high-performance hybrid supercapacitor, *Mater. Today Energy*, 2021, **21**, 100736, DOI: 10.1016/j.mtener.2021.100736.

66 N. Manyani, P. Siwatch, S. Rana, K. Sharma and S. K. Tripathi, Study of electrochemical behaviour of binder-free nickel metal-organic framework derived by benzene-1,3,5-tricarboxylic acid for supercapacitor electrode, *Mater. Res. Bull.*, 2023, **165**, 112320, DOI: 10.1016/j.materresbull.2023.112320.

67 L. Liu, L. Xiong, S. Jiang, Q. Zhao and T. Jiang, Design of high-performance asymmetric supercapacitors (Cu-BDC@Ni1.5Mn0.5-LDH//V2O3/C@Fe0.75Mn0.65O) and study of electrode materials, *J. Energy Storage*, 2024, **75**, 109568, DOI: 10.1016/j.est.2023.109568.

68 J. Yang, C. Zheng, P. Xiong, Y. Li and M. Wei, Zn-doped Ni-MOF material with a high supercapacitive performance, *J. Mater. Chem. A*, 2014, **2**, 19005–19010, DOI: 10.1039/c4ta04346d.

69 R. Bhosale, S. Bhosale, P. Kumbhar, D. Narale, R. Ghaware, C. Jambhale and S. Kolekar, Design and development of a porous nanorod-based nickel-metal-organic framework (Ni-MOF) for high-performance supercapacitor application, *New J. Chem.*, 2023, **47**, 6749–6758, DOI: 10.1039/d3nj00456b.

70 Y. Wu, X. Song, S. Li, J. Zhang, X. Yang, P. Shen, L. Gao, R. Wei, J. Zhang and G. Xiao, 3D-monoclinic M – BTC MOF (M = Mn , Co , Ni) as highly efficient catalysts for chemical fixation of CO 2 into cyclic carbonates, *J. Ind. Eng. Chem.*, 2018, **58**, 296–303, DOI: 10.1016/j.jiec.2017.09.040.

71 B. Dinesh, N. Saravanan and A. S. Kumar, New Strategy for Improved Conductivity and Redox-Enhanced Supercapacitor Performance of Nickel Metal-Organic Framework, *Chem. Eng. J. Adv.*, 2022, **11**, 100311, DOI: 10.1016/j.ceja.2022.100311.

72 B. Iqbal, A. Laybourn, A. ul-Hamid and M. Zaheer, Size-controlled synthesis of spinel nickel ferrite nanorods by thermal decomposition of a bimetallic Fe/Ni-MOF, *Ceram. Int.*, 2021, **47**, 12433–12441, DOI: 10.1016/j.ceramint.2021.01.100.

73 Z. Jiao, Y. Chen, M. Du, M. Demir, F. Yan, W. Xia, Y. Zhang, C. Wang, M. Gu, X. Zhang and J. Zou, 3D hollow NiCo LDH nanocages anchored on 3D CoO sea urchin-like microspheres: A novel 3D/3D structure for hybrid supercapacitor electrodes, *J. Colloid Interface Sci.*, 2023, **633**, 723–736, DOI: 10.1016/j.jcis.2022.11.131.

74 S. Hassanpoor and E. Tamri, FeS2/SRGO nanocomposite: Synthesis, characterization and comprehensive study of supercapacitor behavior in different electrolytes, *J. Alloys Compd.*, 2023, **932**, 167711, DOI: 10.1016/j.jallcom.2022.167711.

75 S. T. Senthilkumar, R. K. Selvan and J. S. Melo, Redox additive/active electrolytes: A novel approach to enhance

the performance of supercapacitors, *J. Mater. Chem. A*, 2013, **1**, 12386–12394, DOI: 10.1039/c3ta11959a.

76 Y. Seo, P. A. Shinde, S. Park and S. Chan Jun, Self-assembled bimetallic cobalt–manganese metal–organic framework as a highly efficient, robust electrode for asymmetric supercapacitors, *Electrochim. Acta*, 2020, **335**, 135327, DOI: 10.1016/j.electacta.2019.135327.

77 D. Acharya, I. Pathak, B. Dahal, P. C. Lohani, R. M. Bhattarai, A. Muthurasu, T. Kim, T. H. Ko, K. Chhetri and H. Y. Kim, Immoderate nanoarchitectures of bimetallic MOF derived Ni–Fe–O/NPC on porous carbon nanofibers as freestanding electrode for asymmetric supercapacitors, *Carbon*, 2023, **201**, 12–23, DOI: 10.1016/j.carbon.2022.08.091.

78 P. Dubey, Mansi, M. Holdynski, A. Deep, U. K. Tiwari, W. Nogala, V. Shrivastav and S. Sundriyal, Unravelling the electrochemistry of Ni-MOF derived nickel phosphide/carbon composite electrode and redox additive electrolyte for high performance supercapacitors, *Mater. Today Chem.*, 2024, **39**, 102165, DOI: 10.1016/j.mtchem.2024.102165.

79 C. Cheng, J. Xu, W. Gao, S. Jiang and R. Guo, Preparation of flexible supercapacitor with RGO/Ni-MOF film on Ni-coated polyester fabric, *Electrochim. Acta*, 2019, **318**, 23–31, DOI: 10.1016/j.electacta.2019.06.055.

80 S. Gao, Y. Sui, F. Wei, J. Qi, Q. Meng and Y. He, Facile synthesis of cuboid Ni-MOF for high-performance supercapacitors, *J. Mater. Sci.*, 2018, **53**, 6807–6818, DOI: 10.1007/s10853-018-2005-1.

81 A. A. Bhoite, K. V. Patil, R. S. Redekar, P. S. Patil, V. A. Sawant and N. L. Tarwal, Solvothermal synthesis of binder free Ni-MOF thin films for supercapacitor electrodes, *J. Solid State Chem.*, 2023, **326**, 124192, DOI: 10.1016/j.jssc.2023.124192.

82 X. Zhang, N. Qu, S. Yang, Q. Fan, D. Lei, A. Liu and X. Chen, Shape-controlled synthesis of Ni-based metal-organic frameworks with albizia flower-like spheres@nanosheets structure for high performance supercapacitors, *J. Colloid Interface Sci.*, 2020, **575**, 347–355, DOI: 10.1016/j.jcis.2020.04.127.

83 T. Mohammadi, M. G. Hosseini, E. Pastor and H. Ashassi-Sorkhabi, One-step growth of RuNi-MOF nanoarrays on carbon felt host as a high-performance binder-free electrode for dual application: Ethanol fuel cell and supercapacitor, *J. Energy Storage*, 2024, **79**, 110146, DOI: 10.1016/j.est.2023.110146.

84 S. Daneshvar and M. Arvand, In-situ growth of hierarchical Ni–Co LDH/CoMoO4 nanosheets arrays on Ni foam for pseudocapacitors with robust cycle stability, *J. Alloys Compd.*, 2020, **815**, 152421, DOI: 10.1016/j.jallcom.2019.152421.

85 A. Enaiet Allah, Three-dimensional N-doped mesoporous carbon–MXene hybrid architecture for supercapacitor applications, *RSC Adv.*, 2023, **13**, 9983–9997, DOI: 10.1039/d2ra06817f.

86 A. Enaiet Allah, H. Tan, X. Xu, A. A. Farghali, M. H. Khedr, A. A. Alshehri, Y. Bando, N. A. Kumar and Y. Yamauchi, Controlled synthesis of mesoporous nitrogen-doped carbons with highly ordered two-dimensional hexagonal mesostructures and their chemical activation, *Nanoscale*, 2018, **10**, 12398–12406, DOI: 10.1039/c8nr02647e.

87 A. E. Allah, Y. Yamauchi, J. Wang, Y. Bando, H. Tan, A. A. Farghali, M. H. Khedr, A. Alshehri, Y. G. Alghamdi, D. Martin, M. A. Wahab, M. S. A. Hossain and A. K. Nanjundan, Soft-Templated Synthesis of Sheet-Like Nanoporous Nitrogen-Doped Carbons for Electrochemical Supercapacitors, *ChemElectroChem*, 2019, **6**, 1901–1907, DOI: 10.1002/celc.201900151.